

Modeling Geometry and Progressive Failure of Material Interfaces in Plain Weave Composites

SU-YUEN HSU AND RON-BIN CHENG

ABSTRACT: A procedure combining a geometrically nonlinear, explicit-dynamics contact analysis, computer aided design techniques, and elasticity-based mesh adjustment is proposed to efficiently generate realistic finite element models for meso-mechanical analysis of progressive failure in textile composites. In the procedure, the geometry of fiber tows is obtained by imposing a fictitious expansion on the tows. Meshes resulting from the procedure are conformal with the computed tow-tow and tow-matrix interfaces but are incongruent at the interfaces. The mesh interfaces are treated as cohesive contact surfaces not only to resolve the incongruence but also to simulate progressive failure. The method is employed to simulate debonding at the material interfaces in a ceramic-matrix plain weave composite with matrix porosity and in a polymeric-matrix plain weave composite without matrix porosity, both subject to uniaxial cyclic loading. The numerical results indicate progression of the interfacial damage during every loading and reverse loading event in a constant strain amplitude cyclic process. However, the composites show different patterns of damage advancement.

INTRODUCTION

Localized inelastic deformation and failure in textile composite materials are sensitive to the internal geometry of the materials. Finite element meso-mechanical progressive damage analysis of textile composites is hindered by difficulties in efficiently creating a realistic model and reducing the number of nodes. The difficulties arise from the contact among the fiber tows, which is ubiquitous in actual textile composites, and from the concurrent thinness and large concaving surface curvature of the volume taken by the matrix.

Most approaches for creating the internal geometry of 2-D (two-dimensional) textile composites with orthogonal fiber tows (such as in plain, twill, and satin weaves) are implemented solely by the CAD (Computer-Aided Design) techniques. Without computing the mechanical interaction among interlacing fiber tows, the CAD-based approaches resort to experimental findings and simplifications. Most CAD-based approaches for 2-D fabrics with orthogonal fiber tows assume that the cross section of each fiber tow is constant and has its first and second lines of symmetry parallel with and normal to the fabric plane, respectively. (In the CAD-based approaches for 2-D fabrics with orthogonal fiber tows, the cross sections of the fiber tows are taken normal to the fabric planes.) The contour of the cross section is basically constructed with an elliptical, circular, or sinusoidal curve and its image with respect to the first symmetry line. Furthermore, the cross section can have truncations parallel with the lines of

symmetry; therefore, the cross section may additionally have two or four straight edges. If the geometry of contacting edges of one fiber tow in an interlacing zone is set identical with the geometry of the centerline of the other tow and vice versa, then a consistent areal contact can be ensured (e.g., [1-5]). Otherwise, complete separation of two interlacing fiber tows is assumed to avoid interpenetration (e.g., [6, 7]). We note that adopting the complete separation results in extended thin layers of matrix between neighboring fiber tows, which can severely increase the nodes of a congruent mesh as a reasonable bound of the element aspect ratio is enforced. A few CAD-based approaches for 2-D fabrics with orthogonal fiber tows employ position-dependent cross sections for the tows. Hivet and Boisse [8] used different asymmetric cross sections for different zones of a fiber tow and incorporated the aforementioned sufficient condition for consistent areal contact. However, the cross sections are still enveloped in a constant rectangle. In [8], CAD solids representing the fiber tows are created as “swept blend.” In the work by Crookston, Ruijter, et al. [9] and Lin, Sherburn, et al. [10], each position-dependent cross section of a fiber tow is defined with splines that pass through a number of points. If the number of points is sufficiently large, interpenetrating tows can be completely separated by adjusting the points (and necessarily, the local fiber volume fraction) at the cross sections in a presumed way. By simple mapping, Tang, Whitcomb, et al. [11] and Goyal and Whitcomb [12] were able to obtain finite element meshes for 2×2 braids, where the non-orthogonal fiber tows have position-dependent asymmetric cross sections, from meshes for 2×2 twills, where the orthogonal fiber tows have constant symmetric cross sections.

Other researchers seek to increase model fidelity or model more complicated fabrics (e.g., stacked 2-D fabrics, fabrics with non-orthogonal fiber tows, 3-D fabrics) by simulating the mechanical interaction among interlacing fiber tows. CAD techniques are also required to at least convert the simulation results into CAD solids. In general, a simulation-based approach using more realistic constitutive models for the tows yields higher fidelity, however, at a greater computational expense. Lomov, Huysmans, et al. [13] and Verpoest and Lomov [14] computed the centerlines and dimensions of the cross sections, either elliptical or lenticular, of the fiber tows from the conditions of equilibrium and continuity. (In the simulation-based approaches, the cross sections of the fiber tows are taken normal to the tow paths.) In their derivation, the fiber tows are treated as elastic shear-deformable beams and experimentally determined relations between the cross-sectional dimensions and the compressive transverse force acting on the tows are used. A very short computational time for a unit cell of a complicated 3-D textile has been reported. We note that in reality, the deformation in the fiber tows is dominated by inelastic shear deformation due to slippage of the fibers. As discussed by Lomov, Ivanov, et al. [15] and Ivanov, Baudry, et al. [16], the method is not immune from interpenetration. In [15], interpenetrating tows are separated by an ad hoc mesh deformation procedure based on the linear finite element formulation of elasticity. The separation can cause the afore-mentioned increase in the size of a congruent mesh. Zhou, Sun, and Wang [17] modeled each tow as a bundle of chains of rod finite elements and performed contact analyses that simulated the kinematic steps of a 2-D weaving process and a 3-D braiding process. Excellent theoretical-experimental correlation of the internal

geometry of the 2-D weave and 3-D braid was reported by Miao, Zhou, et al. [18]. Addressing the computational-time concern, they found that much shortened simulations that started with the tows arranged pursuant to the desired interlacing patterns (textile architecture) and having initially circular cross sections, and omitted the chain-chain friction yielded nearly the same results. It should be noted that the architecture initially cannot fit into the desired unit cells because the rod elements have rigid cross sections. Zhou, Mollenhauer, and Iarve [19] simulated vacuum bag compression of randomly nested layers of a 2-D braided preform and demonstrated a way to build solids from bundles of the deformed chains. One should still expect minor interpenetration problems with these solids. Instead of the rod element, Durville [20] formulated a special beam element that can accommodate the cross-sectional planar strains. The use of the more sophisticated element should conduce to reducing the number of elements per chain and the number of chains per tow. In addition, a special contact algorithm is implemented in [20] to improve performance. It is reported in [21] that it took a cluster of six processors days to complete a simulation for a plain weave where the tows assumed the desired textile architecture from the very beginning.

Most finite element meso-mechanical progressive failure analyses of textile composites were performed on congruent meshes that are conformal with the internal geometry (e.g., [11, 16]). Consistently, emphasis in geometry modeling has been placed on building automated general procedures for generation of congruent conformal meshes (e.g., [14, 22]). Crookston, Ruijter, et al. [9] pointed out difficulties in building such procedures if contact among the fiber tows is allowed. It should be noted that if contact is allowed, the topology for constructing a tow very probably varies from one tow to another and from one set of textile design parametric values to another for the same textile architecture. On the other hand, voxel meshes (volumetric-pixel meshes), which are regular orthogonal meshes and in general are non-conformal, can be generated easily. The original (congruent) version of voxel meshes has been used for meso-mechanical analysis by Ernst, Vogler, et al. [23] and the incongruent version (due to adaptive local refinement) by Kim and Swan [24] and Crookston, Ruijter, et al. [9]. Resolving material inhomogeneity with a voxel mesh incurs a substantial increase in the model size. Moreover, a complication arises from the stairs-like material interfaces in a voxel mesh. Because the interfacial failure criteria and fracture energy increment for a surface element on an actual interface depend on the orientation and size of the surface element, they cannot be computed on a stairs-like substitute. Note that the areal difference between an actual interface and a stairs-like one does not approach zero as the element size is made approach zero.

In this paper, a general method is proposed to create realistic finite element meso-mechanical models of textile composites suitable for progressive failure analysis. Realistic internal geometry of various textile composites can be obtained by simulating the effects of interlacing. To improve the efficiency of the simulation, we use a coarse solid finite element mesh to compute the geometry of the fiber tows and start the computation with the tows having simplified cross sections, arranged in the desired interlacing pattern fit into the target unit cell, and being contact-free. The initial configuration is made possible by setting the initial cross-sectional areas of the

fiber tows smaller than the actual values. Thus, a corrective fictitious thermal expansion is imposed on the tows to cause contact among them during the simulation. The overall efficiency can be further improved by enhancing the reliability of automation. To this end, we choose to directly discretize the computed geometry, where there is ubiquitous tow-tow areal contact, into an incongruent conformal fine mesh for progressive damage analysis. We do not take the mostly used approach, artificially inserting thin layers of matrix between neighboring fiber tows in hope of generating a congruent conformal mesh, because such a mesh usually has a considerable amount of nodes carrying little additional information. The present approach admits mesh incongruence at both tow-tow and tow-matrix interfaces. Recall that in terms of geometry, the matrix is drastically different from the fiber tows. Allowing the tow-matrix mesh incongruence, one can mesh the matrix independently of the fiber tows and therefore has more freedom to reduce the size of a model. In the fine mesh for progressive damage analysis, each material interface (mesh incongruence) is assigned softening traction-separation cohesive contact behavior. Therefore, interfacial failure is consistent with fracture mechanics and immune from the well-known problem of spurious mesh sensitivity. The computed total energy dissipation over a significant interfacial failure is primarily a function of the mode and extent of the failure, not sensitive to mesh density. This suggests that effects of interfacial failure and its interaction with other internal damage on the overall material response may be accurately predicted in the presence of moderate mesh incongruence at the interfaces.

The simple architecture of plain weave is ideal for an initial verification and demonstration of the proposed general method. In the next section, a description of each step of the method is presented, followed by application of the step toward building finite element models of a plain weave composite with matrix porosity and another without matrix porosity. Subsequently, finite element analyses of progressive interfacial cracking in the two composites subject to uniaxial cyclic loading are presented. Most physical quantities in the numerical examples are non-dimensional. Length is normalized by half the thickness of the plain weave under consideration, say, L . Quantities which have the same unit as stress are normalized by the longitudinal Young's modulus of the fiber tows under consideration, say, S . Therefore, energy dissipation per unit area of crack extension is normalized by SL .

GENERATION OF FINITE ELEMENT MODELS

The first step of the proposed method is to obtain the geometry of the fiber tows by nonlinear finite element computation of the internal state of equilibrium. The numerical results are converted into CAD entities and then CAD operations are performed on these entities to construct solids representing the fiber tows and a slightly reduced volume of the matrix in the domain of interest. The solids are meshed individually. Subsequently, nonlinear finite element elasticity-based mesh deformation is applied to adjust primarily the matrix elements to achieve

conformity. Finally, material coordinate systems are assigned to the finite elements for the fiber tows. These steps, illustrated by Figures 1 and 2, are described below.

Step 1- Performing Contact Analysis to Compute Geometry of Fiber Tows

It is assumed that time-consistency of the loading events on the fiber tows is not important for computing the internal geometry, neither is the initial cross-sectional geometry of the tows. The assumptions seem reasonable if 1) at the beginning of the deformation process, the cross-sectional geometry is convex, 2) during the process, no instability occurs, 3) at the end of the process, most of the bounding surfaces of the tows are in contact. Therefore, we attempt to start with an initial configuration that is easy to construct and approximates expected major geometric characteristics of the final configuration. A good choice is to set the fiber tows contact-free and assign them simplified constant cross sections (e.g., elliptical or circular) with moderately reduced areas and simplified tow paths which are arranged in the desired interlacing pattern and fit into the target unit cell. Hence, all the fabric design parameters (e.g., fabric type, tow spacings, and tow lengths in a unit cell) should be used to build the initial configuration. Each fiber tow can be modeled with a coarse mesh composed of cross-sectional layers of quadratic solid finite elements and the centerline of the tow is represented by connected element edges (Step 1 in Figure 1). A fictitious thermal expansion is imposed on the fiber tows in the simulation until the cross-sectional areas reach specified values, which should be consistent with the known longitudinal stiffness of the tows. Virtually, all the boundary conditions and loadings required for the simulation are approximations. For example, inferring from assumed internal periodicity, one may enforce at an end of a fiber tow anti-symmetry of the relative displacements and symmetry of traction, both with respect to the centroid of the end, and constrain the displacements at the centroid to a linear macroscopic displacement field. If the peak stretching load in a fiber tow is assumed, the stretching and relaxation can be simulated by subjecting a tow end to an increasing and then decreasing follower load that is tangential to the tow path at the end. A transversely isotropic and elastic ideal-plastic constitutive model for the fiber tows is used for the simulation. A sufficiently large longitudinal yield stress that does not cause a numerical problem, otherwise arbitrary, can be easily chosen to ensure the entirely elastic longitudinal normal strain. In general, the three shear yield stresses with respect to a principal material coordinate system are small and the shear strains due to interlacing are dominated by plasticity. Therefore, the shear stresses are also small, the shear yield stresses are much lower than the corresponding shear elastic moduli, and the shear yield stresses and shear moduli are unimportant to equilibrium and hence their accuracy is immaterial. Consequently, among the material constants, only the Young's moduli and Poisson's ratios deserve consideration of accuracy.

Step 1 for the plain weave shown in Figure 1 is carried out by explicit dynamic frictionless-contact analysis with the following material parameters for the (unconsolidated) fiber tows: $E_1 = 1$, $E_2 = E_3 = 0.05$, $\nu_{12} = \nu_{13} = 0.2$, $\nu_{23} = 0.3$, $G_{23} = E_2/2(1 + \nu_{23}) = G_{12} = G_{13}$, $\sigma_{11}^y = E_1 \times 40\%$, $\sigma_{23}^y = G_{23} \times 1\% = \sigma_{12}^y = \sigma_{13}^y$, $\sigma_{22}^y = \sigma_{33}^y = 2\sigma_{23}^y$, $\alpha_1 = 0$, and $\alpha_2 = \alpha_3 =$

1°C^{-1} , where E denotes the Young's modulus, ν the Poisson's ratio, G the elastic shear modulus, σ^y the yield stress, and α the coefficient of thermal expansion. In the above, the subscript 1 indicates the longitudinal direction of the fiber tows, and 2 and 3 the two transverse directions. In the example, a rigid wall is placed above the fiber tows and another below to simulate symmetric stacking and compacting. The distance between the two walls is 2. The distance between the two ends (perpendicular to the rigid walls) of each fiber tow is 7.5, which is also the tow spacing. Both initial tow paths are piecewise linear with a length of 3.8. The initial cross-sectional area of each tow is 2.443. The fictitious temperature change is set to 0.4°C . Because of the dominating plastic incompressibility, the final cross-sectional area should be nearly $(e^{0.4})^2 \times 2.443 = 5.437$. Anti-symmetry of the relative displacements and symmetry of the tractions, both with respect to the centroid of each end of the fiber tows, are enforced on the end surface. The centroids of the ends are fixed until the completion of the expansion and then freed to slide in the directions of the fiber tows projected onto the textile plane. The coarse mesh with quadratic tetrahedral elements shown in Figure 1 has 1772 nodes. A computation was performed with the Abaqus[®]/Explicit program running in the 32-bit mode on an Intel[®] Core[™] 2 Duo T9600 processor (2.80 GHz) and took about two minutes. It was found that the effect of the relaxation on the geometry is negligible for the example.

Step 2- Constructing CAD Solids from Deformed Fiber Tows

Due to the mesh regularity, the nodes on the lateral surface of each deformed fiber tow can be easily connected with splines to form closed contours (Step 2 in Figure 1). Then a swept-blend solid is constructed from the contours, with the aid of contingent assumptions of symmetry or anti-symmetry, to represent a segment of a fiber tow that extends beyond the boundaries of the domain for the desired meso-mechanical analysis. For convenience, such a solid is called “standard fiber tow.” For each fiber tow, new points are created by translating its lateral-surface nodes by a small amount in the respective directions normal to the lateral surface of the standard tow and similarly an “enlarged fiber tow” is constructed from the new points. To ensure no matrix pocket between two contacting fiber tows, the enlarged tows will be used as cutters to create solids approximating the matrix (Step 3c in Figure 1). To enlarge the fiber tows shown in Figure 1, which have a thickness of 1, a 0.005 nodal translation is applied. If the matrix has porosity, another solid called “matrix cylinder” is created for each fiber tow by a larger nodal translation. The matrix cylinders will be joined, trimmed, and then cut with the enlarged fiber tows to obtain a solid approximating the porous matrix (Steps 3b and c in Figure 1). For the example in Figure 1, a 0.45 nodal translation is applied to obtain the matrix cylinders.

Steps 3a, b, and c- Constructing CAD Solids for Tows and Matrix in Analysis Domain

Step 3a- constructing solids for tows: The standard fiber tows are trimmed to the boundaries of the domain for the desired meso-mechanical analysis. Without matrix porosity, the analysis domain for the present example is a rectangular parallelepiped whose size is $7.5 \times 7.5 \times 2$.

Step 3b- preparing raw solid for porous matrix: The matrix cylinders are joined and then trimmed to the boundaries of the analysis domain to form the raw solid that will be processed further to obtain a solid representation of the porous matrix.

Step 3c- constructing solid for matrix: The raw solid for the matrix either with or without porosity is cut with the enlarged fiber tows. The result is an approximate solid representation of the matrix because of the use of the enlarged fiber tows as the cutters.

Step 4- Meshing and Assembling

The trimmed standard fiber tows are meshed with quadratic tetrahedral elements. One usually has good control of the number of nodes used for the trimmed standard fiber tows. However, this is seldom true for the matrix due to the concurrent thinness and large concaving surface curvature of the matrix. To eliminate the difficulty, the matrix is meshed with linear tetrahedral elements and then the linear elements are converted into quadratic elements with flat faces. Subsequently, all the meshes are assembled into an incongruent and non-conformal mesh. The resulting mesh would be conformal if gaps and overlaps at the tow-matrix interfaces, attributed to the use of the enlarged fiber tows as the cutters and the flat faces of the matrix elements, could be eliminated by adjusting the matrix elements. The nonporous mesh and porous mesh shown in Figure 1 have 121,338 nodes and 115,006 nodes, respectively. The gaps and overlaps at the tow-matrix interfaces can be seen in the first row of Figure 2, while excellent mesh conformity is seen at the tow-tow interfaces.

Step 5- Mesh Adjustment

Two brief simulations of contact are performed to achieve the desirable mesh conformity. In the first one, a thermal contraction is applied to the boundary elements of each trimmed standard fiber tow to get them clear of the overlaps. Then, by bringing the temperature in the boundary elements of the fiber tows back to the initial temperature, the contraction is recovered and the overlapping matrix elements are pushed back due to contact. Subsequently, a thermal expansion is applied to the boundary elements of the matrix to close the gaps. Boundary nodes of the analysis domain that are near the non-conformity are allowed to slide tangentially in order to eliminate the non-conformity without altering the boundary geometry of the analysis domain. The rest of the boundary nodes can be either fixed or allowed to slide tangentially; the choice should be made on the basis of minimum implementation effort. In addition, all the interior nodes of the fiber tows are fixed. To ensure no net change in the geometry of the fiber tows after the mesh adjustment, the fiber tows should be much stiffer than the matrix. It suffices to assign fictitious isotropic elastic and thermal expansion properties to the constituents. The imposed

contraction and expansion (in terms of strain) can be easily estimated from the thicknesses of the worst overlaps, gaps, and involved elements if a vanishing Poisson's ratio is used for the constituents. The following parameters are used for both meshes in the example: For the fiber tows, $E = 1$, $\nu = 0$, $\alpha = 1^\circ\text{C}^{-1}$; for the matrix, $E = 10^{-3}$, $\nu = 0$, $\alpha = 1^\circ\text{C}^{-1}$; the temperature change for contraction is -0.1°C ; the temperature change for expansion is 0.05°C . All the boundary nodes of the non-porous mesh are allowed to slide tangentially, while all the nodes on the bounding surfaces of the porosity in the other mesh are fixed. The result for the nonporous mesh is illustrated by the second row of Figure 2. As seen in Figure 2, only tiny remnants persist in very limited regions, which can be reduced to a negligible level by the second simulation. The result for the porous mesh is similarly satisfactory.

For the second simulation, the entire model consists of a fictitious homogeneous isotropic material and is subject to a uniform increment in temperature. The only displacement conditions are enforced at the boundary nodes of the analysis domain, the same as for the first simulation. This simple arrangement makes the second mesh adjustment only occur in small neighborhoods of the residual gaps. Therefore, the geometric changes of the fiber tows should be negligible. The following parameters are used for the second mesh adjustment: $E = 1$, $\nu = 0$, $\alpha = 1^\circ\text{C}^{-1}$; the temperature change for expansion is 0.01°C . The effectiveness of the second mesh adjustment of the nonporous mesh is evident in the third row of Figure 2. The second mesh adjustment works as well for the porous mesh.

Step 6- Defining Material Coordinate Systems

The fiber tows in the fine mesh intended for the meso-mechanical analysis are assumed to have transversely isotropic material properties. For each fiber tow, a spline is fitted through the nodes that are located on the centerline of the tow in the deformed coarse mesh in Step 1. To define the axis of transverse isotropy for a finite element of a fiber tow in the fine mesh, the normal projection of the centroid of the element to the spline for the tow is determined first and then the unit vector that is tangential to the spline at the projection. After defining the axis of transverse isotropy with the unit vector, one can establish a principal material coordinate system for the element.

PROGRESSIVE INTERFACIAL CRACKING

To focus on effects of constituent properties, the porous model and non-porous model demonstrated above are used to simulate progressive interfacial cracking in a ceramic-matrix composite (CMC) and a polymeric-matrix composite (PMC), respectively, although the material parameters used in Step 1 are more suitable for the (unconsolidated) fiber tows of the PMC. In addition, the damage inside the tows and matrix is purposely “switched off” in order to isolate implications of the interfacial failure. The interfacial behavior before complete separation (final

failure) is represented by a softening traction-separation cohesive model described below. Damage initiates when the “cohesive-surface quadratic stress criterion” variable (*CSQUADSCRT*) reaches one, i.e., $CSQUADSCRT = 1$. *CSQUADSCRT* is defined by

$$CSQUADSCRT \equiv \sqrt{\left(\frac{\langle t_n \rangle}{t_n^{max}}\right)^2 + \left(\frac{t_s}{t_s^{max}}\right)^2 + \left(\frac{t_t}{t_t^{max}}\right)^2} \quad (1)$$

where t_n , t_s , and t_t denote the three orthogonal traction components acting on an interface, the normal component, first shear component, and second shear component, respectively, and t_n^{max} , t_s^{max} , and t_t^{max} denote the corresponding ultimate strengths. If $t_n < 0$, $\langle t_n \rangle = 0$; if $0 \leq t_n$, $\langle t_n \rangle = t_n$. When damage evolves after the initiation, each mode of the traction-separation response (e.g., normal traction vs. normal separation) follows a softening straight line (as the response envelope) toward the final failure. The area under the envelope for a mode represents the critical density of energy dissipation (energy dissipation per unit area of crack extension) due to that mode of damage. If an unloading occurs at a point on the envelope before the final failure, the response to the unloading follows a linear path toward the origin of the traction-separation plane. The response to a reloading subsequent to the unloading also follows the same linear path until the envelope is reached, and then resumes tracing the softening envelope. The areas under the respective softening envelopes, i.e., critical densities of energy dissipation, are governed by the following quadratic law:

$$\left(\frac{G_n}{G_n^c}\right)^2 + \left(\frac{G_s}{G_s^c}\right)^2 + \left(\frac{G_t}{G_t^c}\right)^2 = 1 \quad (2)$$

where G_n , G_s , and G_t denote the critical densities of energy dissipation due to the normal mode, first shear mode, and second shear mode of damage, respectively, in a general damage process, and G_n^c , G_s^c , and G_t^c denote the critical densities of energy dissipation in the respective pure-mode damage processes. After the final failure of an interfacial area, the two crack surfaces interact with each other through frictionless contact. The cohesive model and post-failure contact described above is commercially implemented in the “contact analysis with cohesive contact properties” within the Abaqus/Explicit program [25]. The analysis set-up is described below.

Porous CMC: For the transversely isotropic (consolidated) fiber tows, $E_1 = 1$, $E_2 = E_3 = 0.952$, $\nu_{12} = \nu_{13} = 0.231$, $\nu_{23} = 0.311$, $G_{12} = G_{13} = 0.376$, $G_{23} = E_2/2(1 + \nu_{23})$; for the isotropic ceramic matrix, $E = 0.676$, $\nu = 0.3$; for both the tow-tow and tow-matrix interfaces, $t_n^{max} = 3.38 \times 10^{-4}$, $t_s^{max} = t_t^{max} = 2.6 \times 10^{-4}$, $G_n^c = 4.07 \times 10^{-7}$, $G_s^c = G_t^c = 1.22 \times 10^{-6}$.

Non-porous PMC: For the transversely isotropic (consolidated) fiber tows, $E_1 = 1$, $E_2 = E_3 = 0.0577$, $\nu_{12} = \nu_{13} = 0.28$, $\nu_{23} = 0.33$, $G_{12} = G_{13} = 0.0356$, $G_{23} = E_2/2(1 + \nu_{23})$; for the isotropic polymeric matrix, $E = 0.026$, $\nu = 0.36$; for both the tow-tow and tow-matrix interfaces, $t_n^{max} = 2.6 \times 10^{-4}$, $t_s^{max} = t_t^{max} = 1.91 \times 10^{-4}$, $G_n^c = 3.34 \times 10^{-6}$, $G_s^c = G_t^c = 1 \times 10^{-5}$.

Boundary conditions: Both finite element models shown in Figure 1 are subject to displacement-controlled uniaxial cyclic loading. The bounding surfaces of the porosity in the CMC model are load-free. For convenience, a face of the CMC model is defined as the union of all the flat boundary surfaces that have the same orientation. Hence, like the PMC model, the CMC model has six faces. For both CMC and PMC, all the six faces are free of tangential traction. The normal displacement is set to zero on the $-x$, $-y$, and $-z$ faces. The normal displacement on the x , y , and z faces are constrained to respective master nodes, one on each face. The total normal load on the y face is zero, so is the total normal load on the z face. A history of the normal displacement (in the x direction) is prescribed at the master node on the x face. For the CMC, the prescribed history corresponds to an overall-strain history that proceeds from 0%, to 0.15%, to -0.15% , and finally to 0.3%. For the PMC, it proceeds from 0%, to 0.6%, to -0.6% , and finally to 1.2%.

A preliminary test is performed to ensure that the non-porous model and the above method for applying uniaxial tensile loading can accurately reproduce a linear displacement field if the material is entirely homogeneous and isotropic. For the test, $\nu = 0.3$ is used and the model is stretched to 0.6% in the x direction. As shown in Figure 3, the numerical results are very accurate.

The computed overall stress and strain responses of the CMC and PMC are presented in Figures 4 and 5. Note that σ_{ij} and ε_{ij} are the overall stress (composite stress) tensor and overall strain (composite strain) tensor, respectively, referencing the Cartesian coordinate systems shown in Figure 1. The two composites show essential similarity in their behavior, including how hysteretic loops form and the subsequent compressive stiffness being between the initial tensile stiffness and first unloading stiffness in terms of magnitude. Over the entire loading history applied to the CMC, the effect of the interfacial damage on every response curve is evident. However, within the leading constant strain amplitude cycling applied to the PMC (from $\varepsilon_{xx} = 0\%$, to 0.6%, to -0.6% , and then back to 0.6%), only the effect on ε_{zz} is evident. Another interesting distinction is the concaving-down curvature of the ε_{yy} - ε_{xx} curve of the PMC.

Contours plots of *CSQUADSCRT* on the bounding surfaces of the fiber tows at different overall strains along the loading history are presented in Figures 6 and 7. The plots clearly indicate the progression of the computed interfacial damage because once *CSQUADSCRT* reaches one (damage initiates) at any interfacial point, its value at that location is fixed to one by the analysis code. Therefore, the areas with the maximum value of one monotonically extend. For convenience, let the fiber tows running in the x direction and y direction called x tow and y tow, respectively, the interface between the x tow and matrix called x -m interface, the interface between the y tow and matrix called y -m interface, and the tow-tow interface called x -y interface. For both composites, the interfacial damage initiates at locations on the y -m interface and x -y interface that are near the “leading edge” (the portion of the lateral surface that contains the large cross-sectional curvature) of the y tow, and at locations on the x -m interface that are across from the leading edge of the underlying y tow. The damage initially propagates faster at the y -m interface and x -y interface in the CMC, while the damage initially propagates faster at the x -m interface in the PMC. The damage evolves during every loading and reverse loading event within

the leading constant strain amplitude cycling for both composites. Recall that for the PMC, within the leading cycling, the apparent effect of the internal damage is only observable from the ε_{zz} response. In fact, the internal damage accumulation is so extensive that it will manifest itself when the composite is subject to a subsequent in-plane shear load.

CONCLUDING REMARKS

The proposed method has the potential to become a general framework for efficiently constructing realistic models for meso-mechanical simulation of complex behavior (such as progressive failure) of various textile composites. For the examples demonstrated above, damage (continuum or discontinuity) models and associated numerical methods for the fiber tows and matrix can be incorporated in order to simulate every aspect of damage evolution and interaction in the plain weaves. The other near-future work should be the application of the method to a stack-up of plain weave layers and other 2-D and 3-D textile architectures.

REFERENCES

1. Thom, H. (1999). Finite Element Modeling of Plain Weave Composites, *Journal of Composite Materials*, 33(16): 1491–1510.
2. Whitcomb, J.D., Tang, X. (2001). Effective Moduli of Woven Composites, *Journal of Composite Materials*, 35(23): 2127–2144.
3. Tang, X., Whitcomb, J.D. (2003). Progressive Failure Behaviors of 2D Woven Composites, *Journal of Composite Materials*, 37(14): 1239–1259.
4. Nicoletto, G., Riva, E. (2004). Failure Mechanisms in Twill-Weave Laminates: FEM Predictions vs. Experiments, *Composites Part A*, 35(7-8): 787–795.
5. Owens, B.C., Whitcomb, J.D., and Varghese, J. (2010). Effect of Finite Thickness and Free Edges on Stresses in Plain Weave Composites, *Journal of Composite Materials*, 44(6): 675–692.
6. Carvelli, V., Poggi, C. (2001). A Homogenization Procedure for the Numerical Analysis of Woven Fabric Composites, *Composites Part A*, 32(10): 1425–1432.
7. Karkkainen, R.L., Sankar, B.V. (2006). A Direct Micromechanics Method for Analysis of Failure Initiation of Plain Weave Textile Composites, *Composites Science and Technology*, 66 (1): 137–150.
8. Hivet, G., Boisse, P. (2005). Consistent 3D Geometrical Model of Fabric Elementary Cell, Application to a Meshing Preprocessor for 3D Finite Element Analysis, *Finite Elements in Analysis and Design*, 42 (1): 25–49.
9. Crookston, J.J., Ruijter, W., Long, A.C., Warrior, N.A., Jones, I.A. (2007). A Comparison of Mechanical Property Prediction Techniques Using Conformal Tetrahedral, In: *Proceedings of Finite Element Modeling of Textiles and Textile Composites*, Saint-Petersburg, Russia.
10. Lin, H., Sherburn, M., Crookston J., Long, A.C., Clifford, M.J., Jones, I.A. (2008). Finite Element Modelling of Fabric Compression, *Modeling and Simulation in Materials Science and Engineering*, 16(3): 035010.
11. Tang, X., Whitcomb, J.D., Kelkar, A.D., Tate, J. (2006). Progressive Failure Analysis of 2×2 Braided Composites Exhibiting Multiscale Heterogeneity, *Composites Science and Technology*, 66 (14): 2580–2590.
12. Goyal, D., Whitcomb, J.D. (2006). Analysis of Stress Concentrations in 2×2 Braided Composites, *Journal of Composite Materials*, 40(6): 533–546.

13. Lomov, S.V., Huysmans, G., Luo, Y., Parnas, R.S., Prodromou, A., Verpoest, I., Phelan, F.R. (2001). Textile Composites: Modelling Strategies, *Composites Part A*, 32(10): 1379–1394.
14. Verpoest, I., Lomov, S.V. (2005). Virtual Textile Composites Software WiseTex, *Composites Science and Technology*, 65(15-16): 2563–2574.
15. Lomov, S.V., Ivanov, D.S., Verpoest, I., Zako, M., Kurashiki, T., Nakai, H., Hirosawa, S. (2007). Meso-FE Modelling of Textile Composites: Road Map, Data Flow, and Algorithms, *Composites Science and Technology*, 67(9): 1870–1891.
16. Ivanov, D.S., Baudry, F., Van Den Broucke, B., Lomov, S.V., Xie, H., Verpoest, I. (2009). Failure Analysis of Triaxial Braided Composite, *Composites Science and Technology*, 69(9): 1372–1380.
17. Zhou, G., Sun, X., Wang, Y. (2004). Multi-chain Digital Element Analysis in Textile Mechanics, *Composites Science and Technology*, 64(2): 239–244.
18. Miao, Y., Zhou, E., Wang, Y., Cheeseman, B.A. (2008). Mechanics of Textile Composites Micro-geometry, *Composites Science and Technology*, 68 (7-8): 1671–1678.
19. Zhou, E.G., Mollenhauer, D., Iarve, E. (2008). Micro-geometric Modeling of Textile Preforms with Vacuum Bag Compression: An Application of Multi-chain Digital Element Technique, *AIAA 2008-1868*.
20. Durville, D. (2005). Numerical Simulation of Entangled Materials Mechanical Properties, *Journal of Materials Science*, 40(22): 5941–5948.
21. Durville, D. (2007). Finite Element Simulation of Textile Materials at Mesoscopic Scale, In: *Proceedings of Finite Element Modeling of Textiles and Textile Composites*, Saint-Petersburg, Russia.
22. Wentorf, R., Collar, R., Shephard, M.S., Fish, J. (1999). Automated Modeling for Complex Woven Mesostructures, *Computer Methods in Applied Mechanics and Engineering*, 172(1-4): 273–291.
23. Ernst, G., Vogler, M., Hühne, C., Rolfes, R. (2010). Multiscale Progressive Failure Analysis of Textile Composites, *Composites Science and Technology*, 70 (1): 61–72.
24. Kim, H.J., Swan, C.C. (2003). Voxel-Based Meshing and Unit-Cell Analysis of Textile Composites, *International Journal for Numerical Methods in Engineering*, 56 (7): 977–1006.
25. *Abaqus 6.9 Analysis User's Manual* (2009), Dassault Systèmes Simulia Corporation, Providence, RI.

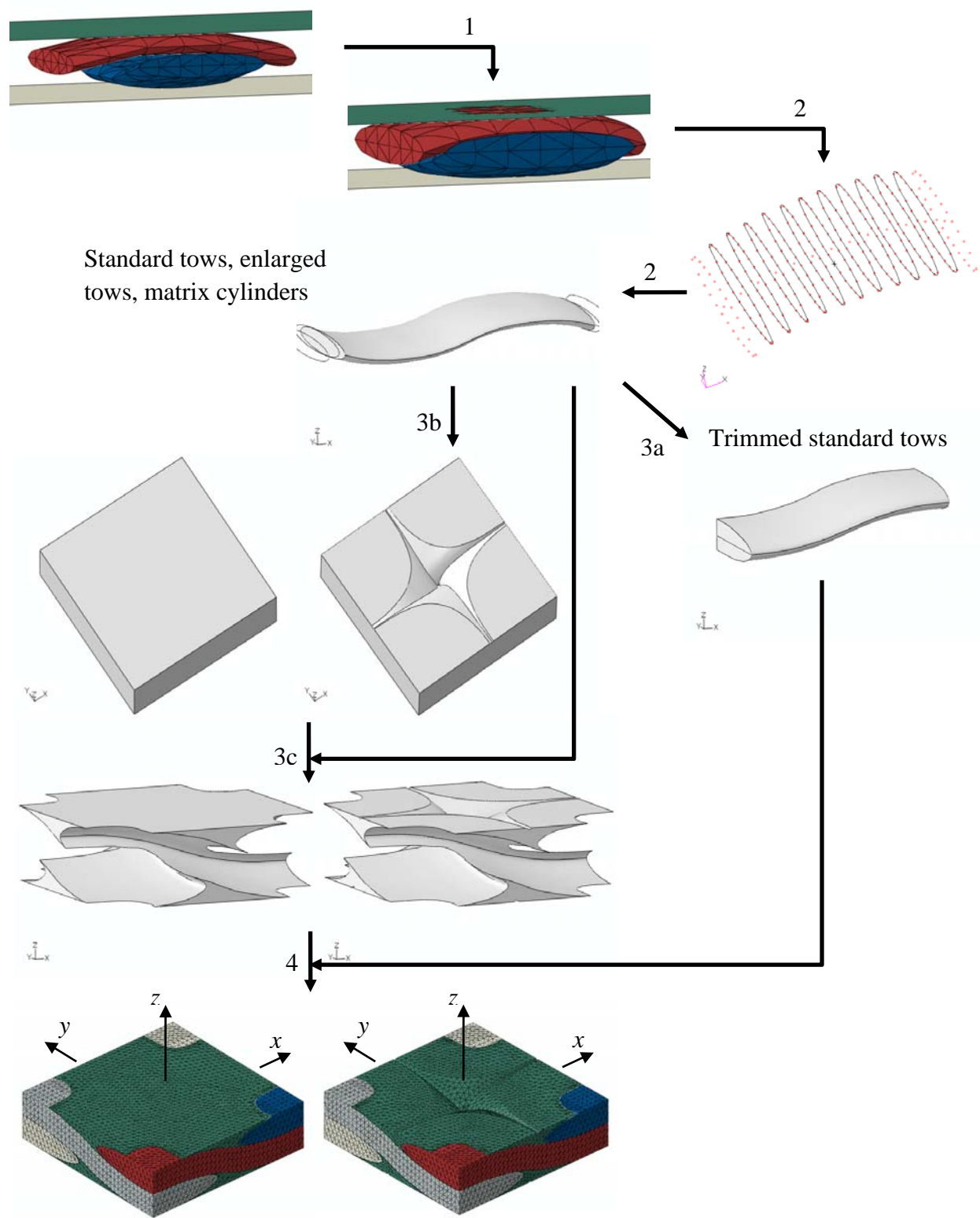


Figure 1. Steps 1-4 for generation of finite element models for textile composites.

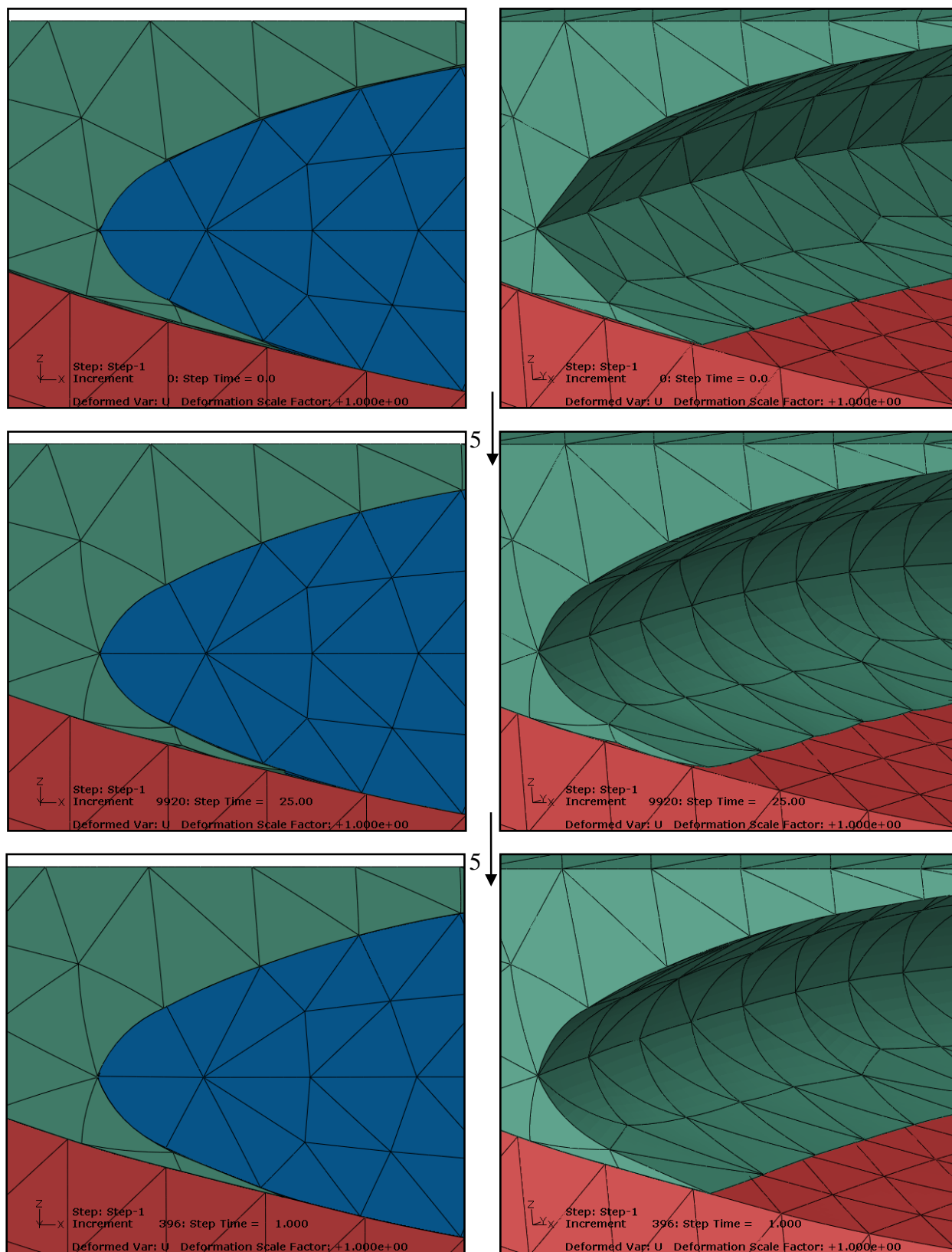


Figure 2. Step 5- mesh adjustment.

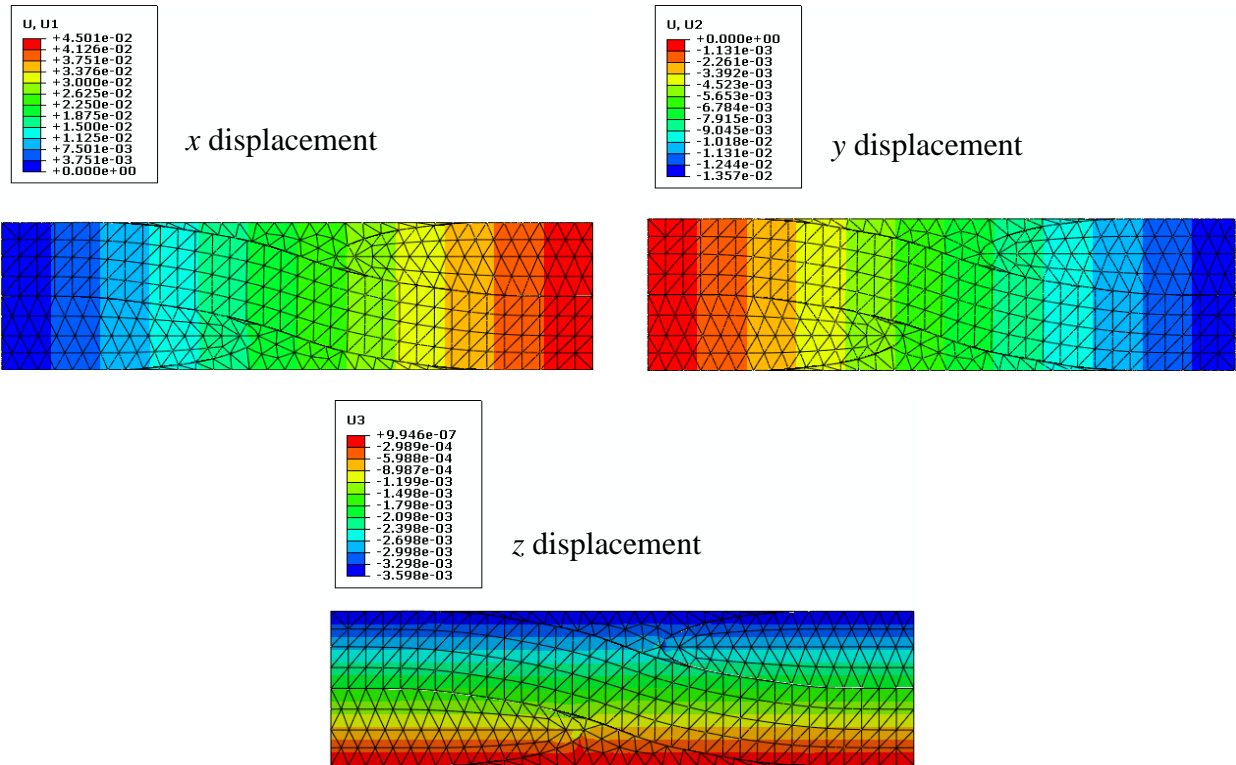


Figure 3. Homogeneous and isotropic material subject to uniaxial tension.

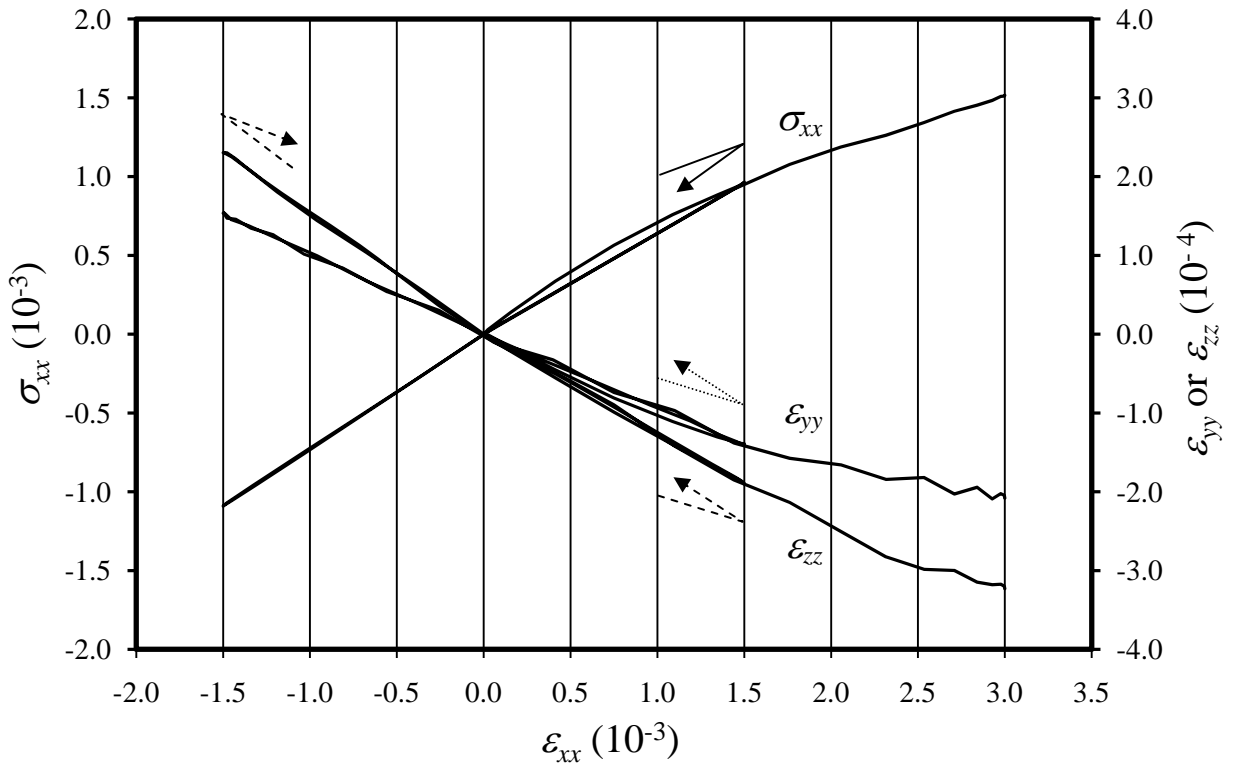


Figure 4. Overall stress and strain responses of plain weave CMC.

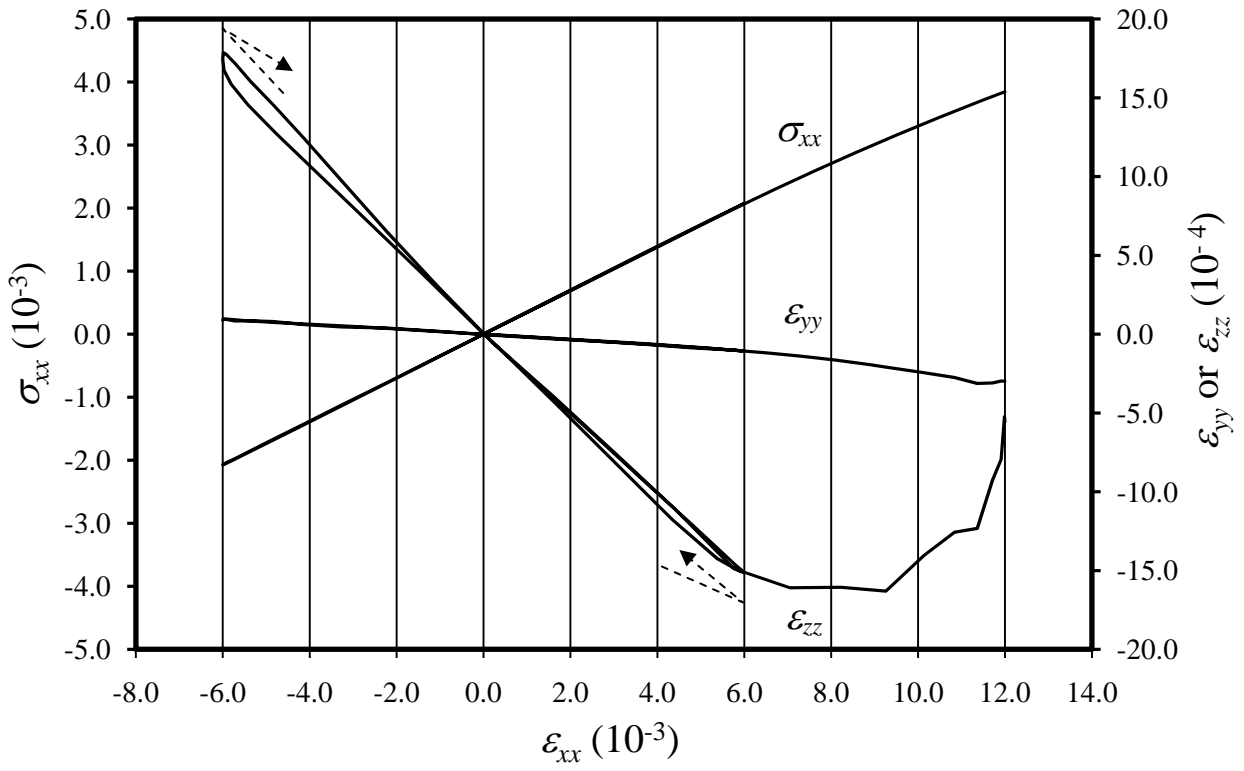


Figure 5. Overall stress and strain responses of plain weave PMC.

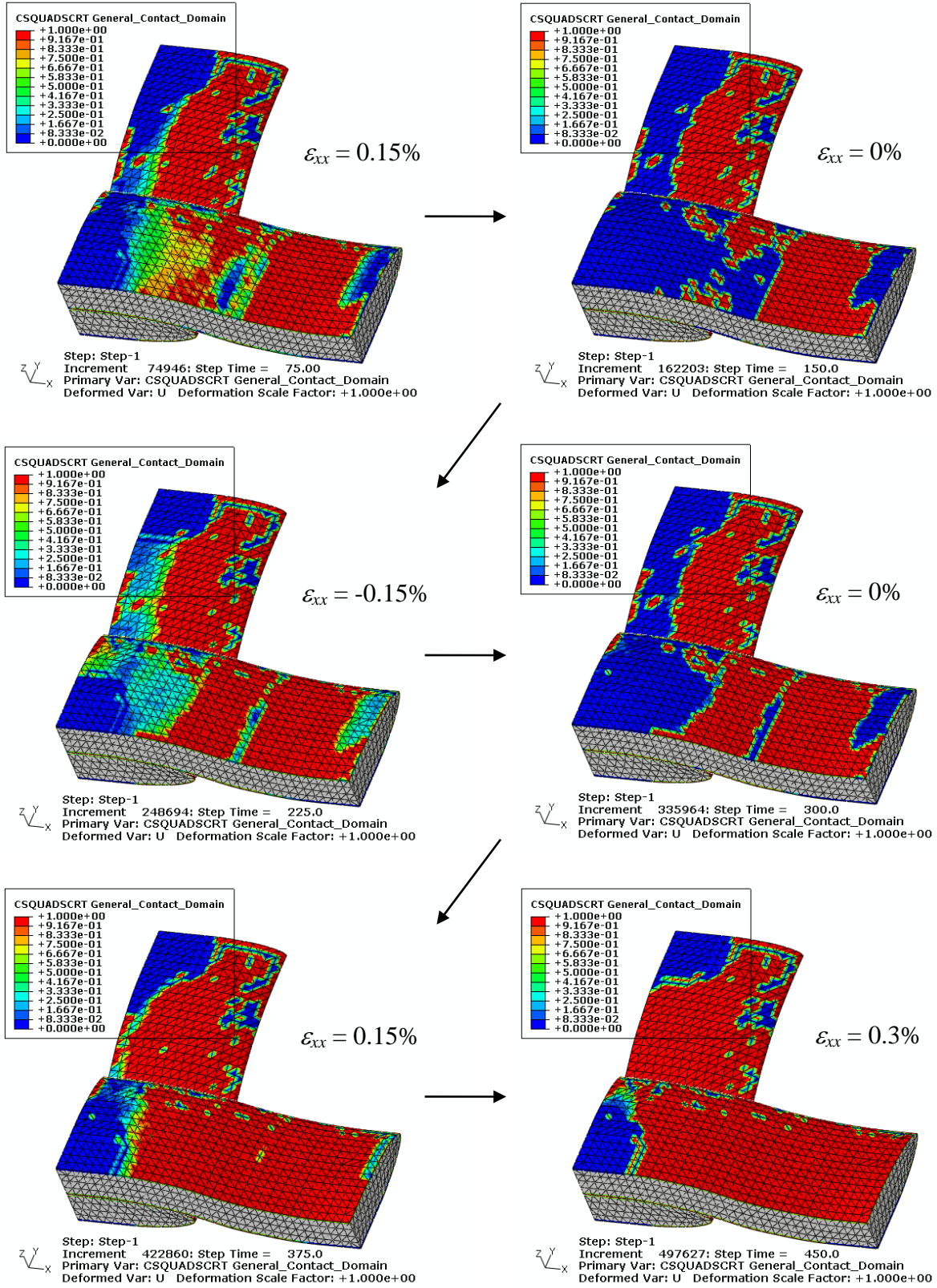


Figure 6. Progressive interfacial failure in plain weave CMC.

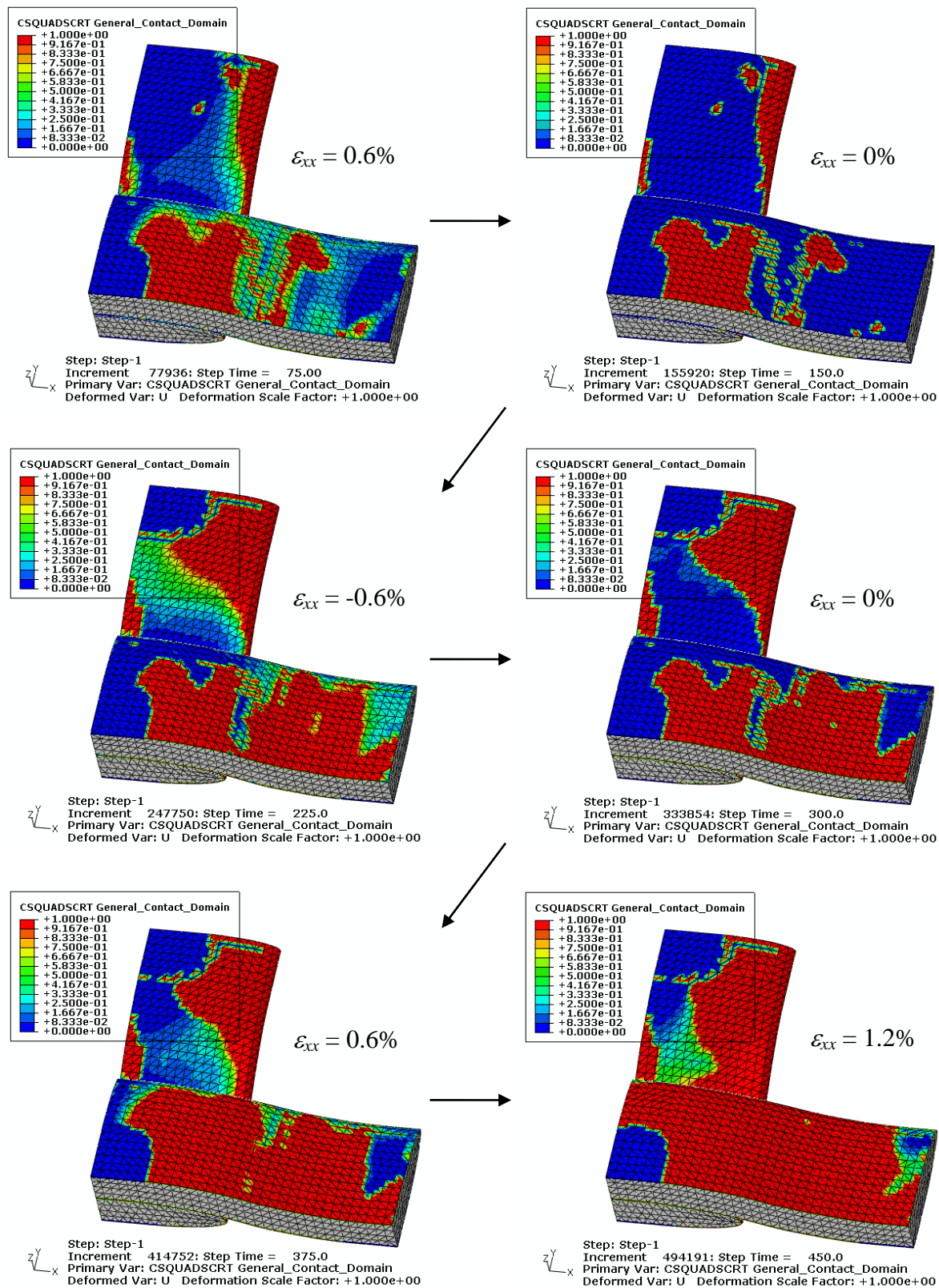


Figure 7. Progressive interfacial failure in plain weave PMC.